Relativistic-electron-driven magnetic reconnection in the laboratory

A. E. Raymond,[1] C. F. Dong,[2] A. McKelvey,[1,3] C. Zulick,[1,*] N. Alexander,[4] A. Bhattacharjee,[2] P. T. Campbell,[1] H. Chen,[3] V. Chvykov,[1,†] E. Del Rio,[4] P. Fitzsimmons,[4] W. Fox,[2] B. Hou,[1] A. Maksimchuk,[1] C. Mileham,[5] J. Nees,[1] P. M. Nilson,[5] C. Stoeckl,[5] A. G. R. Thomas,[1] M. S. Wei,[4] V. Yanovsky,[1] K. Krushelnick,[1] and L. Willingale[1]

[1]*Center for Ultrafast Optical Science, University of Michigan, Ann Arbor, Michigan 48109, USA*
[2]*Princeton Plasma Physics Laboratory, Princeton University, Princeton, New Jersey 08540, USA*
[3]*Lawrence Livermore National Laboratory, 7000 East Ave, Livermore, California 94550, USA*
[4]*General Atomics, 3550 General Atomics Court San Diego, California 92121-1122, USA*
[5]*Laboratory for Laser Energetics, Rochester University, Rochester, New York 14623, USA*

(Received 30 October 2017; revised manuscript received 8 August 2018; published 24 October 2018)

Magnetic reconnection is a fundamental process occurring in many plasma systems. Magnetic field lines break and reconfigure into a lower energy state, converting released magnetic field energy into plasma kinetic energy. Around some of the universe's most energetic objects, such as γ-ray burst or active galactic nuclei, where the magnetic field energy exceeds the plasma rest mass energy, the most extreme magnetic reconnection in the relativistic regime is theorized. The presented experiments and three-dimensional particle-in-cell modeling recreate in the laboratory the scaled plasma conditions necessary to access the relativistic electron regime and therefore approach conditions around these distant, inaccessible objects. High-power, ultrashort laser pulses focused to high intensity ($I > 2.5 \times 10^{18}$ Wcm^{-2}) on solid targets produces relativistic temperature electrons within the focal volume. The hot electrons are largely confined to the target surface and form a radial surface current that generates a huge, expanding azimuthal magnetic field. Focusing two laser pulses in close proximity on the target surface leads to oppositely directed magnetic fields being driven together. The fast electron motion due to the magnetic reconnection is inferred using an experimental x-ray imaging technique. The x-ray images enable the measurement of the reconnection layer dimensions and temporal duration. The reconnection rates implied from the aspect ratio of the reconnection layer, $\delta/L \approx 0.3$, was found to be consistent over a range of experimental pulse durations (40 fs–20 ps) and agreed with the modeling. Further experimental evidence for magnetic reconnection is the formation of a nonthermal electron population shown by the modeling to be accelerated in the reconnection layer.

DOI: 10.1103/PhysRevE.98.043207

I. INTRODUCTION

The phenomenon of magnetic reconnection, the breaking and reconnecting of magnetic field lines in a plasma, can be investigated using laboratory plasmas, such as Tokamaks [1], dedicated experiments such as the magnetic reconnection experiment (MRX) [2], or laser-driven plasmas [3–11]. This enables the study of fundamental energy transfer processes occurring during changes of the magnetic field topology over a wide range of plasma parameters.

Previous laser-driven magnetic reconnection experiments used nanosecond duration laser pulses focused to moderate intensities, $I \simeq 10^{14-15}$ Wcm^{-2}, to interact with a solid target and create two colliding plasmas [3–11]. The perpendicular temperature and density gradients generate azimuthal ~100 T magnetic fields (Biermann battery effect) that are driven together by the bulk motion of the plasma or the heat flux [12–14]. Experiments have measured the rearrangement of the magnetic fields [4], the elevated plasma temperatures in the reconnection region [3,15], and high-velocity plasma jets emanating from the reconnection region [3,7]. Comparisons between these experiments and solar flares [7] and the asymmetric reconnection between the solar wind and the earth's magnetosphere [11] have given new insight. The resulting reconnection fields are predicted to accelerate electrons to energies exceeding the plasma's thermal energy [16], and enable the investigation of scaled phenomena in astrophysical objects [17–20]. Numerical modeling of relativistic intensity laser pulses creating a magnetic annihilation or reconnection geometry have been reported from near-critical plasma [21], underdense plasma [22,23], or in a microscale plasma slab [24].

However, the extremely energetic class of astrophysical phenomena, including high-energy pulsar winds, γ-ray bursts, and jets from galactic nuclei [25–27], where the energy density of the reconnecting fields exceeds the rest-mass energy density (cold electron magnetization parameter, $\sigma_{\text{cold}} \equiv B^2/(\mu_0 n_e m_e c^2) > 1$) [28], has been inaccessible in the laboratory. This is the regime of relativistic reconnection, which results in much higher energies of accelerated electrons due to the longer confinement time of the charged particles within the acceleration region [29].

The higher-intensity conditions, $I > 10^{18}$ Wcm^{-2}, accessible using femtosecond or picosecond duration laser systems

*Present address: Plasma Physics Division, U.S. Naval Research Laboratory, Washington, DC 20375, USA.
†Present address: ELI-Alps, Szeged, Pintér József Utca, 6728 Hungary.

generate a dense relativistic electron plasma within the focal volume when interacting with a solid target. In this regime, magnetic field generation and transport is primarily governed by relativistic electron dynamics [30]. A previous experiment using the HERCULES laser demonstrated that the expansion of the hot electron plasma rapidly sets up a sheath field at the target-vacuum interface, forcing the majority of the electrons to expand radially along the target surface [31]. These currents generate an azimuthal magnetic field with $\sim 10^4$ T magnitude measured expanding radially at $v_B \sim c$ [31], distinct from the nanosecond pulse regime. Focusing two such high-intensity laser pulses in close proximity creates a reconnection geometry similar to the previous nanosecond laser-driven studies, but with plasma characteristics we will show to be accessing the relativistic reconnection regime ($\sigma_{\text{cold}} > 1$).

Here, we present experimental and three-dimensional (3D) particle-in-cell (PIC) modeling data as evidence for magnetic reconnection driven by relativistic electrons. We show that across a significant range of laser pulse durations, from 40 fs–20 ps, the high-intensity-laser-driven reconnection layer dimensions, and consequently reconnection time, scale with focal spot separation. This implies the dominant physics is the same across the investigated parameters. An x-ray (copper K_α) imaging technique enabled visualization of the fast electrons accelerated in the reconnection region to provide spatial information about the extent of the current sheet, as well as allowing time-resolved measurements of the x-ray emission and hence reconnection timescales. Measurements of the electron spectra provide evidence of the generation of a nonthermal electron population during the reconnection event. Simulations elucidate the relationship between the relativistic energy electron population dynamics, the magnetic field generation, transport, and reconnection along with the associated electric fields.

This paper is organized as follows. Section II presents the experimental geometries on the two laser systems used for the study and the experimental data. The HERCULES facility produced 40 fs duration laser pulses whereas the OMEGA EP facility provided 20 ps laser pulses. However, the focused intensity of both facilities was similar and produced signatures with a striking scaling of the features associated with the reconnection layer (Sec. II A). Furthermore, as described in Sec. II B, the longer pulse durations enabled temporal measurements that are currently impossible on the 40 fs timescales. Section II C presents evidence for the development of a nonthermal electron population, a recently discussed reconnection signature in a laser-driven geometry [16]. Three-dimensional particle-in-cell modeling is presented in Sec. III. This shows the generation and expansion dynamics of the magnetic field, followed by the interaction and reconfiguration during reconnection. The aspect ratio of the current sheet agrees well with the experimental features as well as the development of the nonthermal electron spectra. Finally, in the vicinity of the reconnection region, the magnetization parameter exceeds unity.

II. EXPERIMENTS

Experiments were performed at both the HERCULES laser facility at the University of Michigan ($\lambda = 800$ nm, 2 J, 40 fs pulses focused to FWHM radius of 9 ± 2 μm, intensity of 2×10^{19} Wcm^{-2} at normal incidence), and the OMEGA EP laser facility at the Laboratory for Laser Energetics ($\lambda = 1.053$ μm, 500 J / 1000 J, 20 ps pulses focused to FWHM radius 13 ± 1 μm, intensity of 1.2×10^{18} Wcm^{-2} / 2.5×10^{18} Wcm^{-2} at 57.2° incidence). The experiments focused two short-pulse laser beams onto copper foil targets to spots separated by a distance X_{sep}. The single HERCULES beam used a parabolic mirror cut in half and mounted on a translation stage with a deformable mirror to achieve two focal spots with variable X_{sep} onto 12 μm thick foils. The two OMEGA EP short-pulse beams were fired simultaneously onto 50 μm thick foils. A generalized experimental schematic and diagram of the two-spot field geometry with corresponding magnetic and electric fields is depicted in Fig. 1.

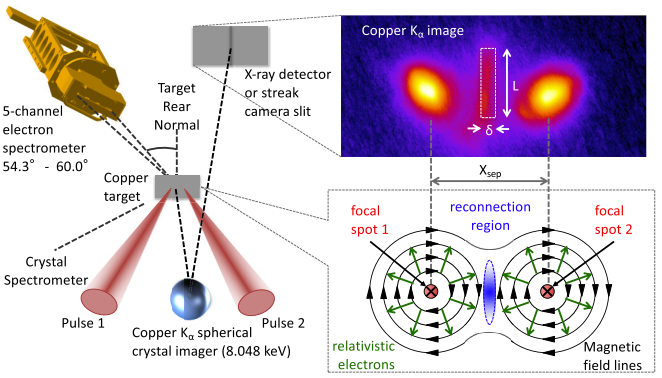

FIG. 1. A schematic of the experimental geometry for the OMEGA EP experiments (similar to the HERCULES setup). The spherical crystal images x-rays from the front side of the target onto a detector. A typical K_α image is shown with the reconnection layer highlighted in the dashed box with of length (L) and width (δ) labeled. A physical picture of the interaction illustrates the two azimuthal magnetic fields expanding into the reconnection region where a target normal electric field accelerates the electrons into the dense target to generate the copper K_α emission in the midplane.

A. Copper K_α imaging of the reconnection layer

When the antiparallel magnetic fields meet in the midplane, $\frac{1}{2}X_{\text{sep}}$, between the interaction sites, the field lines can break and reconnect within the reconnection layer, deflecting inflowing electrons and supporting an electric field in the target-normal direction. This localized electric field generates a current sheet, with electrons being accelerated into the dense regions of the plasma. These fast electrons undergo ionizing collisions with atoms in the target and K-shell electrons are emitted. K_α x-ray emission occurs as these electrons recombine on femtosecond timescales. Therefore, imaging the front side copper K_α (8.048 keV) emission with a spherically bent quartz x-ray crystal [32,33] produced a time-integrated map of the current sheet generated between the magnetic field regions to diagnose the reconnection region.

An Andor iKon BR-DD CCD was used as the detector for the HERCULES experiment, whereas image plate detector was used at OMEGA EP. The spatial resolution of the images for the HERCULES setup was 15 μm and 10 μm for the OMEGA EP setup.

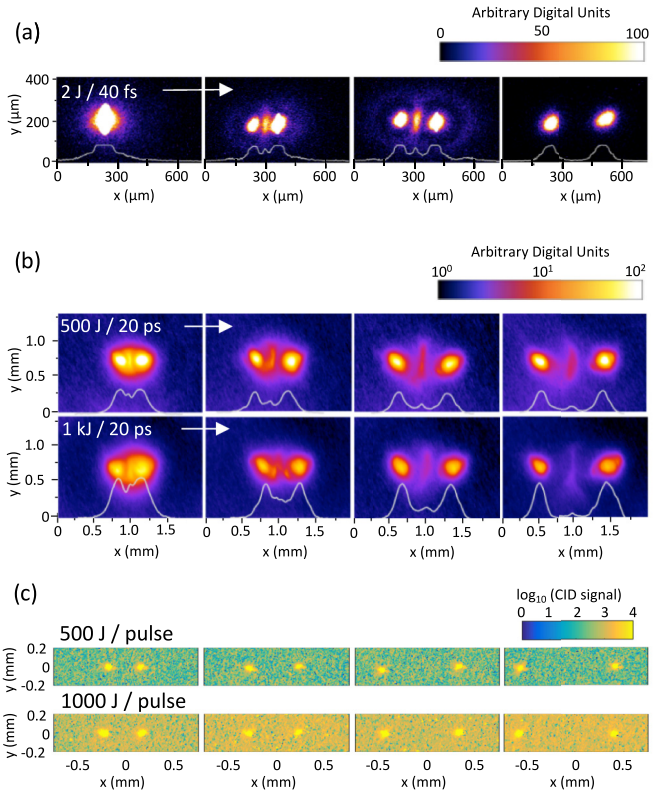

FIG. 2. Front-side copper K_α images from focal spot separation scans using (a) the HERCULES laser and (b) the OMEGA EP laser. Horizontal line-outs from the central 50 μm regions are superimposed. (c) The x-ray (2–6 keV) pinhole camera images from the OMEGA EP shots.

Separation scans of the focal spots were performed with both laser systems and the resulting copper K_α images are shown in Figs. 2(a) and 2(b). Two bright K_α sources corresponding to the x-ray emission due to ionization within the focal volume were observed on both systems. The HERCULES data shown is saturated in these regions to better observe the midplane signal. A separation-dependent enhancement of the K_α radiation at $\frac{1}{2}X_{\text{sep}}$ was also measured corresponding to the current sheet. The midplane emission is ~10% of the signal from the focal spot regions. The signal at $\frac{1}{2}X_{\text{sep}}$ for simultaneously arriving pulses is much greater than the sum of the signal from the pulses fired separately. OMEGA EP pulses deliberately delayed by 100 ps with respect to one another also did not produce any signal in the midplane. Figure 2(c) shows the x-ray pinhole camera images are sensitive to a range of x-ray energies (between 2–6 keV) that depends on the plasma temperature. For the 500 J per pulse shots, the x-ray signal is two orders of magnitude above the background. No midplane emission enhancements are observed in these x-ray pinhole camera images, precluding collisional heating between the two plasmas as a source of the K_α enhancement.

Linear trends were observed for both the length L and width δ of the reconnection region versus focal separation, X_{sep} [Fig. 3(a)], with $L(\mu\text{m}) \approx 0.5 \times X_{\text{sep}}(\mu\text{m})$ and $\delta(\mu\text{m}) \approx 0.15 \times X_{\text{sep}}(\mu\text{m})$ on both systems. This indicates a high reconnection rate defined by the aspect ratio $\delta/L \approx 0.3$ (assuming no compression). The relative strength of

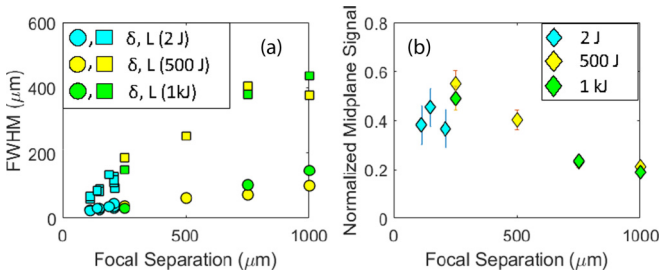

FIG. 3. The enhanced midplane signal FWHM width (δ) and length (L) (left) and integrated signal (right) normalized to the per-shot average of the integrated signal density from the focal spot regions.

reconnection current formed should be proportional to the midplane signal. Figure 3(b) presents the integrated midplane signal normalized to the per-shot average of the integrated signal in the focal spot regions. From both facilities, this data indicates that smaller separations yield stronger reconnection features, until the point when reconnection is suppressed due to a more sensitive dependency upon slight beam mistimings or target deformation. At larger separations, the integrated midplane intensity decreases as the amount of magnetic energy to dissipate is reduced. The reconnection region features have a linear scaling across a wide range of focal separations across the broad range of pulse durations and pulse energies. Therefore, in this laser intensity regime, where relativistic energy electrons are generating the magnetic field and leading the interaction, we infer the physics governing the interaction is comparable and primarily driven by the laser intensity.

B. Temporal measurements

Additional measurements using OMEGA EP (1 kJ, 20 ps) were made using specially designed targets to isolate the signal from the midplane region. Aluminum frames (50 μm thick, 3 mm × 2 mm) were inset with a 50 μm thick copper bar, as shown in Fig. 4. To ensure the radially expanding surface electrons were not impeded by significant surface imperfections or magnetic fields generated by resistivity gradients [34], a 10 μm layer of aluminum/boron was sputtered onto the front surface. The focal positions for $X_{\text{sep}} = 500$ μm or $X_{\text{sep}} = 750$ μm are indicated on Fig. 4(a), positioned symmetrically on either side of the copper bar's long axis. The angle of incidences onto these targets were 51°

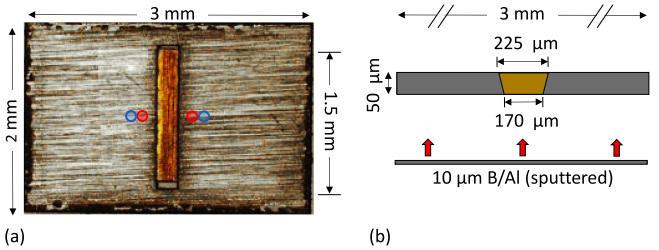

FIG. 4. Targets designed for making temporal measurements. (a) The front side of the target before the sputtering of a 10 μm layer of Al/B showing the location of the Cu bar and the focal positions for the $X_{\text{sep}} = 500$ μm or $X_{\text{sep}} = 750$ μm indicated by the two sets of circles. (b) A cross section showing the dimensions of the Cu bar.

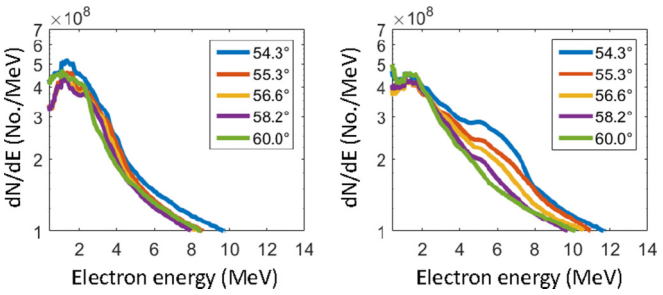

FIG. 5. The electron spectra (for 500 μm separation) from the OMEGA EP multichannel spectrometer at angles from the transmitted laser axis in the case of a 100 ps pulse-to-pulse delay (no reconnection expected, left plot) and no pulse-to-pulse delay (reconnection expected, right plot). Angles are given with respect to the rear target normal.

(pulse 1, P1) and 28.6° (pulse 2, P2). The copper K_α image of the bar was positioned along the entrance slit of an ultrafast x-ray streak camera [35] to observe the temporal duration of the midplane signal.

The streak camera images were averaged, and smoothed using a three-pass pseudo-Gaussian function to produce line-outs. The full-width-at-half-maximum (FWHM) duration of the copper K_α emission are inferred from these line-outs. For shots where only one laser pulse was fired to the position equivalent to a separation of $X_{\text{sep}} = 500$ μm, P1 did not produce a measurable signal and the signal P2 only had a FWHM of (25 ± 2) ps. The FWHM duration for $X_{\text{sep}} = 500$ μm was (27 ± 2) ps and for $X_{\text{sep}} = 750$ μm was (22 ± 2) ps. For 20 ps pulses fired onto a copper foil target pulse durations were measured to be (24 ± 2) ps or 28 ± 2 ps. Therefore, the reconnection signal is of the order the laser pulse duration.

Simultaneously, an absolutely calibrated von Hamos crystal spectrometer [36] measured the K-photon spectra and angularly resolved electron spectra was measured [37]. For the $X_{\text{sep}} = 500$ μm focal spot positions, simultaneous firing of P1 and P2 resulted in 2 ± 0.2 times more photons compared to the sum of the signals from the individual pulse shots. The normalized K_β/K_α photon yield ratio is dependent on the emission region plasma temperature due to the populations available for the $L \rightarrow K$ and $M \rightarrow K$ electronic transitions [38,39], so a higher plasma temperature produces lower K_β/K_α ratios. The single laser pulse shots produced a $K_\beta/K_\alpha = 0.5 \pm 0.1$ corresponding to a temperature of $k_B T_e \approx 160$ eV, whereas the two laser pulse shots produced a $K_\beta/K_\alpha = 0.9 \pm 0.1$ corresponding to $k_B T_e \approx 90$ eV. This implies that for a single pulse interaction, the fast electrons deposit their energy in a hotter plasma, likely on the target surface. In contrast, the reconnection fields produced when both laser pulses are fired drive the fast electrons into the cooler plasma beneath the target surface.

C. Nonthermal electron spectra measurements

Additionally, a five-channel electron spectrometer viewing the rear side of the target observed significant changes to the electron energy distribution with the electron spectra shown in Fig. 5. A quasi-Maxwellian electron energy distribution, typical of laser-solid interactions, was observed when there was a 100 ps pulse-to-pulse delay on target. When the two laser pulses arrived on target concurrently, a nonthermal feature appeared superimposed onto the quasi-Maxwellian energy distribution, consistent with the reconnection electric field accelerating the electrons through the target. There is some variation over the different viewing angles, with the nonthermal contribution increasing at angles closer to the target normal direction. The redistribution of the particle energy in the reconnection fields would preferentially accelerate the electrons in the rear target normal direction.

Therefore the experimental results show evidence for magnetic reconnection from several perspectives: a consistent, localized enhancement of K_α emission from the focal midplane; a short duration of this emission; evidence that the K photons originate from deep within the target; and electron spectra consistent with nonthermal acceleration of electrons in the midplane region. By varying the focal spot separation, the conditions of reconnection are seen to be varied in a controlled manner.

III. PARTICLE-IN-CELL MODELING

A 3D simulation of the reconnection scenario resembling the HERCULES experimental parameters was conducted using the PIC code OSIRIS [40] using 25,200 nodes of the NASA Pleiades supercomputer. The simulated parameters chosen were similar to the HERCULES experiment with a FWHM laser pulse duration of $\tau_p = 20$ fs focused to a peak normalized vacuum vector potential of $a_0 = 3$ (intensity of 2×10^{19} Wcm^{-2}). The box dimensions were $X_1 \times X_2 \times X_3 = 185c/\omega_0 \times 388c/\omega_0 \times 776c/\omega_0$ with a resolution of six cells per c/ω_0 and $3 \times 3 \times 3$ particles per cell. The pulse was normally incident along the X_1 direction at a position a third of the way along the X_2 direction and centered in the X_3 direction upon an electron plasma with $n_{\text{max}} = 30 n_{\text{crit}}$ (where $n_{\text{crit}} = \epsilon_0 m_e \omega_0^2/e^2$ is the critical plasma density), preplasma scale length $l = \lambda$. The electrons had an initial thermal distribution of $k_B T_e/m_e c^2 = 0.01$ and with stationary ions. Periodic boundary conditions in the X_2 direction resulted in an effective spot-to-spot separation of 388 c/ω_0 (50 μm, for $\lambda = 810$ nm). The geometry can be seen in Fig. 6, with $X_2 = 0$ being the midplane between the laser spot and the second effective laser spot through the periodic boundary condition. In the X_1 and X_3 directions, thermal boundaries were used for the particles and open boundaries were used for the fields.

A quasi-Maxwellian population of electrons with $\approx$0.8 MeV temperature was generated from the interaction site(s) after irradiation [41,42], followed by confinement of fast electrons along the plasma surface. The maximum azimuthal B-field magnitude within the interaction site is 3500 T and then falls off as $1/r$ as the electrons propagate along the target surface in the X_2-X_3 plane [31,43,44]. The counterstreaming surface electrons and their associated azimuthal magnetic fields begin to reach the midplane within two pulse durations, when rapid reconnection of the magnetic field lines within a region of $\delta/L \approx 0.35$ was observed from the time-averaged $E_1 \cdot J_1$.

The source of the electric fields can be identified by considering the potentials $\mathbf{E} = -\frac{\partial \mathbf{A}}{\partial t} - \nabla\phi$. Choosing to use the Coulomb gauge, $\nabla \cdot \mathbf{A} = 0$, then the electrostatic potential, ϕ is related to the free charge density, ρ, by

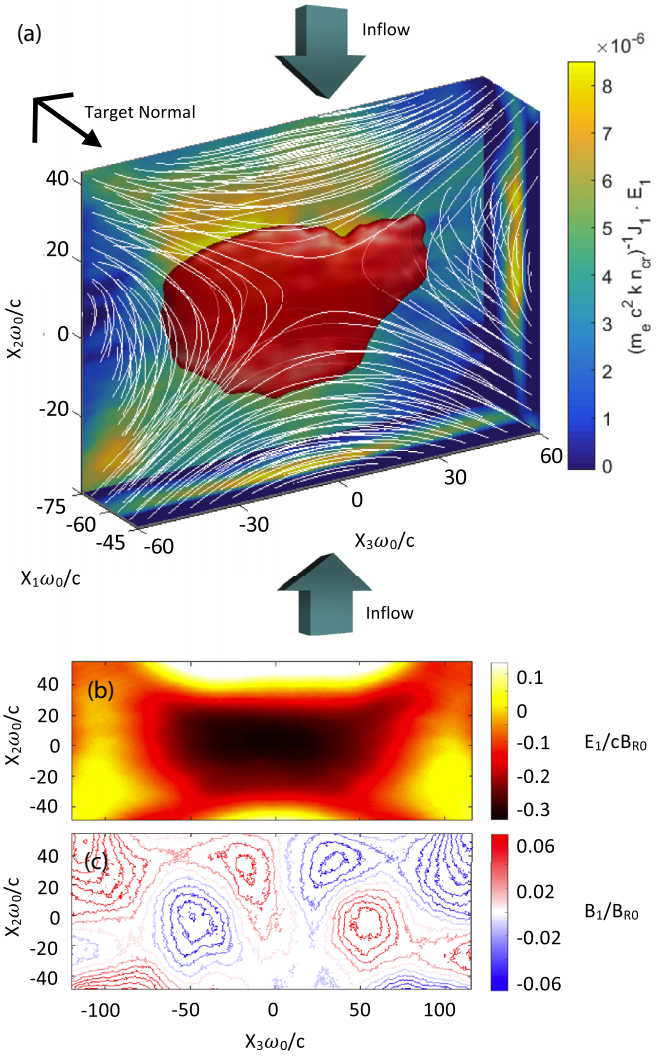

FIG. 6. (a) A 3D graphic of magnetic field streamlines (white lines) illustrating the inflow (and outflow) of the magnetic energy. The associated reconnection electric field [displayed as an isosurface (red online) with magnitude $E_1/cB_{R0} \approx 0.133$], and the value of $E_1 \cdot J_1$ evaluated in center cuts through the displayed volume (box faces). The interaction sites are located 194 c/ω_0 away along x_2, and x_1 is in the target-normal direction. (b) The target normal electric field (charge separation field subtracted) and normalized to cB_{R0}. (c) The magnetic field in the target normal direction normalized to B_{R0}, illustrating the formation of a quadrupole magnetic field pattern. All data is shown at a time of $520.8/\omega_0$ into the simulation.

Poisson's equation and is guaranteed to be unique providing the electric field satisfies the boundary conditions. Therefore, the latter contribution to **E**, the electric field associated with the charge separation responsible for confining the electrons to the target surface, can be subtracted from the overall field to isolate the first term. Therefore the inductive electric field associated with the magnetic field can be isolated in the simulation. As antiparallel magnetic field lines converged and began to reconnect, an out-of-plane electric field with $E_{1,\mathrm{peak}}/cB_{R0} \approx 0.3$ formed, where $B_{R0} \approx 200$ T is the azimuthal magnetic field magnitude in the vicinity of the reconnection layer.

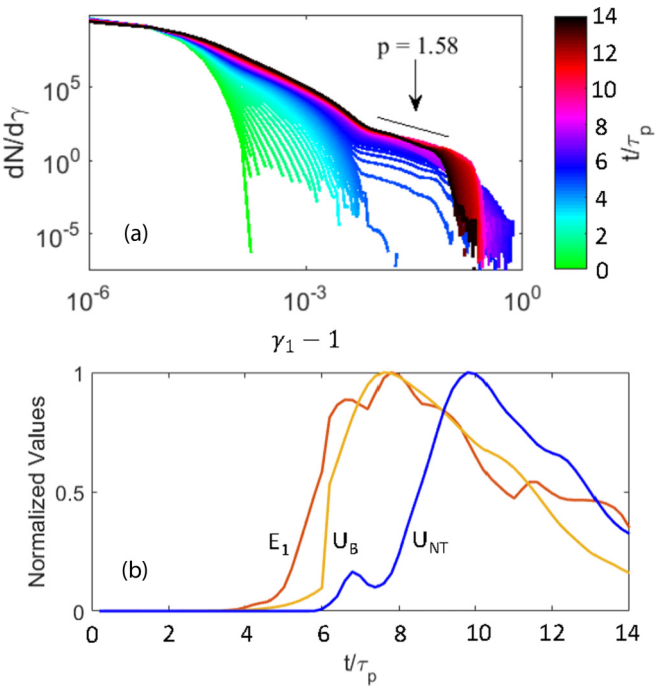

FIG. 7. (a) The temporal evolution of the electron energy spectrum in the x_1 direction $(\gamma_1 - 1)$ within the midplane region, acquiring a hard power-law spectrum once reconnection begins. (b) The temporal behavior of the maximum reconnection electric field magnitude (E_1), magnetic energy (U_B), and the energy in nonthermal electrons (U_{NT}), evaluated in the reconnection region (all quantities are normalized to their respective maximum values). The simulation pulse duration is $\tau_p = 20$ fs.

Figure 6(a) shows a 3D graphic of the magnetic field streamlines (white lines) entering the region, from the focal regions above and below. The electric field associated with the reconnection is shown as a red isosurface for $E_1/cB_{R0} \approx 0.133$. The normalized electric field is equivalent to the rate of reconnection, and matches the experimentally observed value as measured from the current sheet aspect ratio. A localized current sheet with an aspect ratio of $\delta/L \approx 0.3$ at $t = 11\tau_p$ and thickness of ~ 2 μm has dimensions comparable to the midplane electric field. The values of $E_1 \cdot J_1$ evaluated through the center of the displayed volume are displayed on the box faces of Fig. 6(a). Evaluating $E_1 \cdot J_1$, a measure of the work done on the electrons, in the midplane region shows a localization of work done on electrons in the target normal direction [Fig. 6(a)].

Furthermore, an out-of-plane quadrupole magnetic field pattern develops [shown in Fig. 6(c)], characteristic of Hall-like reconnection [45] or electron-magnetohydrodynamics (eMHD) reconnection models [46–48]. Electrons are accelerated into the target (the x_1 direction), and develop a nonthermal spectral component in addition to a quasi-Maxwellian low-energy portion. This can be seen in Fig. 7(a), where the temporal evolution of the electron energy spectrum in the x_1 direction $(\gamma_1 - 1)$ plotted. The data was integrated over a region that is $50c/\omega_0$ in the x_2 direction and centered on the midplane. The nonthermal component may be fitted by a power law $dN/d\gamma \propto \gamma^{-1.58}$, is consistent with that for

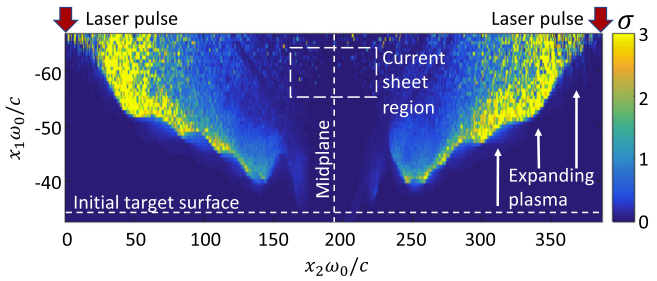

FIG. 8. The calculated σ_{cold} in a 2D slice perpendicular to the target surface along the axis between the two focal spots. The initial target surface position is indicated with a dashed line, arrows indicate the laser pulse interaction positions and the plasma expands into the vacuum from these positions. The midplane between the two focal spots and the approximate region of the current sheet are also overlaid.

relativistic reconnection [49]. A simple estimate of the expected electron energy gain in the reconnection region can be made by noting that $E_1 \sim cB_{R0} \approx 6 \times 10^{10}$ V/m and assuming a thickness of $d \approx 2$ μm to calculate the energy gained to be $E_1 d \sim 120$ keV [i.e., $(\gamma_1 - 1) \sim 0.25$]. This agrees with the spectra shown in Fig. 7(a).

Figure 7 (b) depicts the temporal evolution of three simulation variables: the total magnetic energy density within the reconnection region, the maximum value of the reconnection electric field within this same region, and the energy in the nonthermal portion of the spectra presented in Fig. 7(a). The temporal FWHM of the temporally tracked variables is approximately four pulse durations, demonstrating the rapid conversion of magnetic energy into particle kinetic energy. Both the short reconnection time and observation of the nonthermal electron spectral component is in reasonable agreement with the experimental data.

The magnetization parameter was calculated from the simulation data in some regions to be $\sigma_{\text{cold}} > 10$. The variation of the value of σ_{cold} across a two-dimensional slice through the center of the simulation is shown in Fig. 8. The target surface is at the bottom of the figure and the laser interaction sites are at the edges of the box. The plasma expands from the target surface and travels towards the midplane (indicated with a dashed white line). Approaching the reconnection region, the plasma conditions give $\sigma_{\text{cold}} > 1$, indicating that the relativistic regime is being accessed. The interaction is characterized by a plasma beta of $\beta_e = P_{\text{plasma}}/P_{\text{magnetic}} \sim 50$ and electron skin depth $c/\omega_{pe} = 2.4\,\mu\text{m} < l$ (the current sheet length). 96% of the electron gyroradii $r_g = m_e v_\perp/|q|B$ are smaller than δ.

IV. CONCLUSION

The experimental copper K_α imaging provided a visualization of the fast electron being redirected by the reconnection fields. This enabled the measurement of the reconnection layer dimensions (δ, L) and the linear trend between the focal spot separation and these dimensions to be observed. The measured experimental dimensions are in good agreement with the current sheet dimensions observed in the simulations. The constant δ/L ratio across the range of parameters investigated is consistent with fast reconnection theory. The measurement of the duration of the midplane copper K_α signal implies a fast reconnection rate and the comparison of the K_β/K_α photon ratios suggest the electrons are directed into the cold target for the reconnection configuration. The nonthermal electrons observed for the reconnection configuration further confirm the presence of reconnection fields. The relativistic reconnection regime is indicated by the plasma $\sigma_{\text{cold}} \gtrsim 1$ in the vicinity of the reconnection region in the simulation.

Further investigations are needed to confirm the experimental magnetic field and plasma density conditions and the theoretical expectations in this regime. The magnetic fields can be characterized using proton radiography [43], however, this requires an additional high-energy, picosecond laser pulse to drive the diagnostic. Plasma density measurements will be particularly challenging due to the large gradients and high peak densities. Modifications for Ohm's law in the relativistic limit have been developed [50] and would be required to expand theoretical work to make predictions in this regime where magnetic field connection is nontrivial [51].

The use of two extremely intense laser pulses are a test bed for conducting relativistic reconnection experiments, with the conditions of reconnection controllably varied by adjusting parameters including the beam separation and energies. It may be possible to access even more extreme laboratory regimes in the future with higher magnetic fields or even to generate a dense relativistic electron-positron plasma [52] using the next-generation of 10-Petawatt laser facilities such as ELI-Beamlines [53]. Studying magnetic reconnection from laser-generated electron-positron plasmas will even closer replicate the conditions in the vicinity of galactic nuclei jets, pulsar winds, or γ-ray bursts to give deeper insight into these energetic events where quantum electrodynamics effects such as radiation reaction can be significant [54].

ACKNOWLEDGMENTS

This material is based upon work partially supported by the Department of Energy National Nuclear Security Administration under Award No. DE-NA0002727. The authors gratefully acknowledge technical assistance from the Laboratory for Laser Energetics, and appreciate the use of NASA's High End Computing Capability. The authors would also like to acknowledge the OSIRIS Consortium (UCLA, IST Portugal) for the use of the OSIRIS 2.0 framework, Grant No. NSF ACI 1339893. H.C. was supported under the auspices of the US Department of Energy by Lawrence Livermore National Laboratory under Contract DE-AC52-07NA27344.

[1] J. A. Goetz, R. N. Dexter, and S. C. Prager, Phys. Rev. Lett. **66**, 608 (1991).

[2] M. Yamada, H. Ji, S. Hsu, T. Carter, R. Kulsrud, N. Bretz, F. Jobes, Y. Ono, and F. Perkins, Phys. Plasmas **4**, 1936 (1997).

[3] P. M. Nilson *et al.*, Phys. Rev. Lett. **97**, 255001 (2006).
[4] C. K. Li, F. H. Séguin, J. A. Frenje, J. R. Rygg, R. D. Petrasso, R. P. J. Town, O. L. Landen, J. P. Knauer, and V. A. Smalyuk, Phys. Rev. Lett. **99**, 055001 (2007).
[5] P. M. Nilson *et al.*, Phys. Plasmas **15**, 092701 (2008).
[6] L. Willingale *et al.*, Phys. Plasmas **17**, 043104 (2010).
[7] J. Zhong *et al.*, Nat. Phys. **6**, 984 (2010).
[8] Q.-L. Dong *et al.*, Phys. Rev. Lett. **108**, 215001 (2012).
[9] G. Fiksel, W. Fox, A. Bhattacharjee, D. H. Barnak, P.-Y. Chang, K. Germaschewski, S. X. Hu, and P. M. Nilson, Phys. Rev. Lett. **113**, 105003 (2014).
[10] M. J. Rosenberg, C. K. Li, W. Fox, A. B. Zylstra, C. Stoeckl, F. H. Séguin, J. A. Frenje, and R. D. Petrasso, Phys. Rev. Lett. **114**, 205004 (2015).
[11] M. J. Rosenberg, C. K. Li, W. Fox, I. Igumenshchev, F. H. Séguin, R. P. J. Town, J. A. Frenje, C. Stoeckl, V. Glebov, and R. D. Petrasso, Nat. Commun. **6**, 6190 (2015).
[12] L. Willingale *et al.*, Phys. Rev. Lett. **105**, 095001 (2010).
[13] A. S. Joglekar, A. G. R. Thomas, W. Fox, and A. Bhattacharjee, Phys. Rev. Lett. **112**, 105004 (2014).
[14] W. Fox, A. Bhattacharjee, and K. Germaschewski, Phys. Rev. Lett. **106**, 215003 (2011).
[15] M. J. Rosenberg, J. S. Ross, C. K. Li, R. P. J. Town, F. H. Séguin, J. A. Frenje, D. H. Froula, and R. D. Petrasso, Phys. Rev. E **86**, 056407 (2012).
[16] S. R. Totorica, T. Abel, and F. Fiuza, Phys. Rev. Lett. **116**, 095003 (2016).
[17] B. Remington, D. Arnett, R. P. Drake, and H. Takabe, Science **284**, 1488 (1999).
[18] D. D. Ryutov, R. P. Drake, and B. A. Remington, Astrophys. J. Suppl. Ser. **127**, 465 (2000).
[19] S. V. Bulanov, T. Zh. Esirkepov, D. Habs, F. Pegoraro, and T. Tajima, Eur. Phys. J. D **55**, 483 (2009).
[20] T. Zh. Esirkepov and S. V. Bulanov, ECLA **58**, 7 (2012).
[21] Y. L. Ping, J. Y. Zhong, Z. M. Sheng, X. G. Wang, B. Liu, Y. T. Li, X. Q. Yan, X. T. He, J. Zhang, and G. Zhao, Phys. Rev. E **89**, 031101 (2014).
[22] G. A. Askar'yan, S. V. Bulanov, F. Pegoraro, and A. M. Pukhov, Comments Plasma Phys. Controlled Fusion **17**, 35 (1995).
[23] Y. J. Gu, O. Klimo, D. Kumar, Y. Liu, S. K. Singh, T. Zh. Esirkepov, S. V. Bulanov, S. Weber, and G. Korn, Phys. Rev. E **93**, 013203 (2016)
[24] L. Yi, B. Shen, A. Pukhov, and T. Fülöp, Nat. Commun. **9**, 1601 (2018).
[25] Y. Lyubarsky and J. G. Kirk, Astrophys. J. **547**, 437 (2001).
[26] C. Thompson, Mon. Not. R. Astron. Soc. **270**, 480 (1994).
[27] B. F. Liu, S. Mineshige, and K. Ohsuga, Astrophys. J. **587**, 571 (2003).
[28] M. Melzani, R. Walder, D. Folini, C. Winisdoerffer, and J. M. Favre, Astron. Astrophys. **570**, A111 (2014).
[29] J. G. Kirk, Phys. Rev. Lett. **92**, 181101 (2004).
[30] A. E. Raymond, Ph.D. thesis, University of Michigan, 2016.
[31] W. Schumaker *et al.*, Phys. Rev. Lett. **110**, 015003 (2013).
[32] J. A. Koch *et al.*, Rev. Sci. Instrum. **74**, 2130 (2003).
[33] C. Stoeckl, G. Fiksel, D. Guy, C. Mileham, P. M. Nilson, T. C. Sangster, M. J. Shoup, and W. Theobald, Rev. Sci. Instrum. **83**, 033107 (2012).
[34] A. P. L. Robinson and M. Sherlock, Phys. Plasmas **14**, 083105 (2007).
[35] P. M. Nilson *et al.*, APS DPP, Abstract JO5:00001 (2012).
[36] J. Lu, K. W. Hill, M. Bitter, L. Delgado-Aparicio, N. A. Pablant, P. Efthimion, P. Beiersdorfer, H. Chen, K. Widmann, and M. Sanchez del Rio, *Advances in Computational Methods for X-Ray Optics III* (SPIE, Bellingham, 2014).
[37] J. Zheng, K. A. Tanaka, T. Sato, T. Yabuuchi, T. Kurahashi, Y. Kitagawa, R. Kodama, T. Norimatsu, and T. Yamanaka, Phys. Rev. Lett. **92**, 165001 (2004).
[38] G. Gregori *et al.*, Contrib. Plasma Phys. **45**, 284 (2005).
[39] P. M. Nilson, W. Theobald, J. Myatt, C. Stoeckl, M. Storm, O. V. Gotchev, J. D. Zugel, R. Betti, D. D. Meyerhofer, and T. C. Sangster, Phys. Plasmas **15**, 056308 (2008).
[40] R. A. Fonseca *et al.*, *Proceedings of the International Conference on Computational Science - Part III* (Springer-Verlag, Berlin, 2002), p. 342–351.
[41] S. C. Wilks, W. L. Kruer, M. Tabak, and A. B. Langdon, Phys. Rev. Lett. **69**, 1383 (1992).
[42] C. Zulick, B. Hou, F. Dollar, A. Maksimchuk, J. Nees, A. G. R. Thomas, Z. Zhao, and K. Krushelnick, New J. Phys. **15**, 123038 (2013).
[43] G. Sarri *et al.*, Phys. Rev. Lett. **109**, 205002 (2012).
[44] S. Mondal *et al.*, Proc. Natl. Acad. Sci. USA **109**, 8011 (2012).
[45] D. A. Uzdensky and R. M. Kulsrud, Phys. Plasmas **13**, 062305 (2006).
[46] S. V. Bulanov, Phys. Fluids B: Plas. Phys. **4**, 2499 (1992).
[47] H. Cai and D. Li, Phys. Plasmas **15**, 032301 (2008).
[48] A. N. Simakov and L. Chacón, Phys. Rev. Lett. **101**, 105003 (2008).
[49] F. Guo, H. Li, W. Daughton, and Y.-H. Liu, Phys. Rev. Lett. **113**, 155005 (2014).
[50] F. Pegoraro, Phys. Plasmas **22**, 112106 (2015).
[51] F. A. Asenjo and L. Comisso, Phys. Rev. Lett. **114**, 115003 (2015).
[52] C. P. Ridgers, C. S. Brady, R. Duclous, J. G. Kirk, K. Bennett, T. D. Arber, A. P. L. Robinson, and A. R. Bell, Phys. Rev. Lett. **108**, 165006 (2012).
[53] B. Rus *et al.*, Proc. SPIE **9515**, 95150F (2015).
[54] S. V. Bulanov, Plasma Phys. Controlled Fusion **59**, 014029 (2017).